Vibrational overtones and rotational structure of HCl in rare gas matrices

V. Berghof
Institut für Experimentalphysik, Freie Universität Berlin, Germany

M. Martins
Universität Hamburg, Institut für Experimentalphysik, Germany

B. Schmidt
Fachbereich für Mathematik, Freie Universität Berlin, Germany

N. Schwentner
Institut für Experimentalphysik, Freie Universität Berlin, Germany

(Received 24 January 2002; accepted 13 March 2002)

The rotational structure in the vibrational transitions from $v=0$ to $v=1$, 2, 3, 4 of $H^{35}Cl$ and $H^{37}Cl$ is studied in Xe, Kr, and Ar matrices with high spectral resolution. A consistent set of rotational constants B_v for the vibrational levels $v=0$ to 4 is derived. B_0 decreases with the tightness of the cage from 9.78 cm^{-1} in Xe to 8.83 cm^{-1} in Ar for $H^{35}Cl$ (gas phase 10.44 cm^{-1}). The values for B_0 to B_4 decrease linearly with v due to the vibration-rotation-coupling constant α which increases from 0.37 cm^{-1} in Xe to 0.479 cm^{-1} in Ar (gas 0.303) according to the cage tightness. The splitting of the $R(1)$ transition which originates from the hindering of rotation is analyzed in Xe using the $T_{2g}-T_{1u}$ and $T_{2g}-E_g$ transition energies. A comparison with force field calculations yields a dominant contribution of the sixth spherical harmonic $Y^6_{A_{1g}}$ of the octahedral matrix potential. The modulation of the potential takes a value of $K_6/B=17$ which corresponds to a barrier for the rotation of 160 cm^{-1}. The splitting increases with the vibrational level v which can be interpreted as a weak admixture of the $Y^4_{A_{1g}}$ spherical harmonic. A large isotope effect and a reduction of the $T_{1u}-A_{1g}$ transition energy [$R(0)$-transition] beyond the crystal field value are attributed to an eccentric rotation with a displacement of the center-of-mass of the order of 0.05 Å. The vibrational energies ω_e show an opposite trend with matrix atom size and decrease with polarizability from 2970 cm^{-1} in Ar to 2945.4 cm^{-1} in Xe (gas 2989.9 cm^{-1}) while the anharmonicity $\omega_e x_e$ of the free molecule lies close to the Kr value and thus between that of Ar and Xe. © *2002 American Institute of Physics.* [DOI: 10.1063/1.1475752]

I. INTRODUCTION

Hydrogen compounds belong to the few classes of molecules which show rotation in the condensed phase. Halham stated already in 1973 in his comprehensive review that hydrogen chloride is the most thoroughly investigated stable molecule in solid matrices.[1] The prominent $R(0)$ and $P(1)$ lines in the vibrational spectra indicate the rotation of the molecule. The splitting of these lines which is determined by the rotational constant of the molecule was used to analyze the coupling of rotational and vibrational modes to the rare gas lattices. The fcc lattice of the surrounding noble gas atoms induces a potential field of octahedral symmetry for the molecule in a substitutional site. It has been shown that such a potential can be described by a complete series of Laguerre-polynomials $Y^0_{A_{1g}}$, $Y^4_{A_{1g}}$, $Y^6_{A_{1g}}$, $Y^8_{A_{1g}}$, ... with A_{1g} symmetry.[2] Devonshire[3] has already in 1935 solved the problem of the rotation for a linear molecule in an octahedral field using only the $Y^4_{A_{1g}}$-term to describe the potential.[4] The derived barriers for rotation K_4/B in units of the rotational constant B for HCl in matrices led to inconsistencies in comparison with the available experimental rotational structure at that time.[1]

The asymmetric charge distribution in the HCl-molecule causes a deviation of the center-of-mass from the center of the site. This center of interaction which in Ar is 0.1–0.4 Å apart from the center-of-mass is considered to be the center of rotation of the molecule. The resulting rotation-translation coupling (RTC) predicts the experimentally available energies and separations between the $R(0)$, $R(1)$, and $P(1)$ bands. However, to explain the experimentally observed additional splitting of the $R(1)$ line, crystal field contributions also had to be invoked.[1] The strong dependence of the rotational linewidth on the matrix temperature[5] suggests a strong coupling between the rotational motion and local phonon modes. The RTC-model was used to calculate the decay of vibrational modes to librational modes.[5,6] The severe discrepancies to the experimental vibrational lifetimes[7,8] with orders of magnitude to high relaxation rates were reduced by including intramolecular anharmonicity[6] and by treating the rotational motion quantum mechanically.[9]

The orientation of the H atom with respect to the lattice influences its exit probability in photochemical experiments. A time dependent modeling of the process in a density matrix technique revealed a strong contribution of the $Y^6_{A_{1g}}$ spherical harmonic besides $Y^0_{A_{1g}}$ and $Y^4_{A_{1g}}$ to the HCl-matrix-potential.[10] A dominant $Y^6_{A_{1g}}$ contribution was found also in a

close coupled wave packet approach by deriving rotational wave functions of HCl/DCl in argon.[11]

On the experimental side the vibrational overtones exciting directly the vibrational levels $v=2$ (Ref. 7) and 3 (Ref. 8) have been studied. The spectra were recorded by detecting the fluorescence from the vibrational $v \rightarrow v-1$ decay while scanning the excitation wavelength. These experiments delivered a very fascinating nonradiative relaxation kinetic. Splittings of some rotational lines were observed. However, the evaluation was focused on the matrix influence on the vibrational frequency and anharmonicity. We extend the overtone spectroscopy up to the $v=4$ vibrational level. A systematic analysis of the $R(0)$ and $P(1)$ splittings versus vibrational level yields B values with high accuracy. A significant isotope effect is observed in the matrix in contrast to the gas phase. With the B values the energy of the pure vibrational transition (Q-branch) and the rotation-vibration-coupling constant α are also determined. Giradet and coworkers investigated in a series of papers the interaction of dopants.[12–16] Besides the identification of di- and polymers,[13,17] also the manifestation of interactions between separated HCl molecules resulting in the appearance of the Q-branch is demonstrated in Refs. 12 and 15. The Q-branch is forbidden for the freely rotating molecule and it originates from HCl molecules whose rotational motion is hindered. It will be shown that the Q-branch can therefore not be used for a derivation of precise B values. Finally, the rotational fine structure in a Xe matrix and especially the splitting of the $J=2$ level [$R(1)$ branch] are presented for $v=1$, 2, and 3. Crystal field calculations according to Ref. 2 using a potential set up by the spherical harmonics $Y^4_{A_{1g}}$ and $Y^6_{A_{1g}}$ have been carried out for comparison with the experimental data. They show that the $Y^6_{A_{1g}}$ function is the major contribution in the interaction potential in agreement with the predictions in Ref. 11.

The above-mentioned isotope effect can be related to the rotation of the center-of-mass around the center of interaction. Therefore this contribution to B can be determined directly and compared with the crystal field effects. According to studies for CO in Ar done by Manz,[18] the eccentric motion may lead to a displacement of the surrounding matrix atoms.

II. EXPERIMENT

The HCl doped rare gas films were condensed in an ultrahigh vacuum chamber on a gold coated copper substrate which was cooled by a closed cycle refrigerator to temperatures around 13 K. Optically clear samples with a thickness of typically 0.5 mm were grown within 30 min. The thickness was monitored by interference fringes and the growth rate was controlled by the gas pressure. The gases with nominal purities of HCl: 99.9990%, Ar: 99.99990%, Kr: 99.996%, and Xe: 99.998% from Linde were premixed without further purification in a stainless steel UHV chamber. The chamber was passivated first with a HCl to rare gas ratio of 1:100 and then flushed twice with the desired mixture. After that the HCl concentration in the chamber remains unchanged for weeks.

TABLE I. Efficiency η of the UV/VIS-dyes and the Raman-shifter used in this work vs wavelength λ.

	Dye-laser		Raman-shifter		
Dye[a]	λ	η	Order	λ	η
DCM	652 nm	29%	3	3.47	0.3%
Styryl7	717 nm	20%	2	1.77	5%
Styryl9	801 nm	17%	1	1.2	10%
Styryl14	930 nm	10%	⋯	⋯	⋯

[a]All dyes dissolved in propylencarbonate.

The HCl concentration and the composition with respect to monomers and dimers were probed in absorption by the fundamental vibration transition with a FTIR spectrometer from Bruker (IFS 55 Equinox), which provides a resolution of 0.5 cm^{-1} and an accuracy of 0.01 cm^{-1}. The IR beam was focused by a combination of two 90° parabolic mirrors ($f=300$ and $f=400$ mm) and a plane mirror onto the sample. The reflected beam was imaged by another 90° parabolic mirror ($f=100$) on the LN_2 cooled MCT detector.

The concept for the spectroscopy of the $v=0$ to $v=2$, 3, 4 transitions employs a tunable dye laser with a Raman shifter to scan the different wavelength regions of the overtones and to monitor the fluorescence intensity of the $\Delta v=1$ IR emission as a measure for the absorption probability. The main problem in this experiment is the strongly decreasing absorption cross section σ of the higher overtones. For the gas phase we estimate from the transition strength[19] and the linewidth[20] values of σ (in cm^{-2}) decreasing from 1.5×10^{-18} for $1\leftarrow0$ to 3.9×10^{-20} for $2\leftarrow0$ and 3.2×10^{-22} for $3\leftarrow0$.

A dye laser (FL 2002, Lambda Physik) was pumped with a Nd:YAG laser (Quantel, Brilliant) at 10 Hz and a pulse energy of 150 mJ via a telescope. The optimized pump optics leads to efficiencies (Table I) which exceed the literature values[21] in general and provides an increased lifetime of the dyes. The wavelength reading of the dye laser was calibrated optogalvanically (OCU_{puls} from LAS) with Ne gas lines including the correction for air pressure (≈0.2 nm). Thus we obtained an accuracy of 0.1 cm^{-1}. The Raman shifter (RS 75, Lambda Physik) with a length of 940 mm containing a quartz capillary of 0.7 mm inner diameter was operated between 5 and 15 bars of H_2. The dye laser light was focused via two plane mirrors and a $f=300$ mm BK7 lens into the entrance of the capillary. The overall efficiency was optimized concerning imaging, H_2 pressure, and combination of dye/Raman order (Table I). It may be surprising that shorter wavelength dyes together with higher Raman orders were used to generate the longer wavelength IR light. However, the higher efficiency of the dye and of the Raman process at shorter pump wavelength compensates for the loss in gain with higher order. The Raman orders were finally separated by a Pellin–Broca prism and imaged by a $f=500$ lens onto the sample. The fluorescence was collected with a CaF_2 lens ($f=25$ mm, diameter 1 in.) inside the sample chamber and focused after passing a MgF_2 window by a second CaF_2 lens on a LN_2 cooled InSb detector. Including the back-reflection from the Au substrate a collection efficiency of 13% was

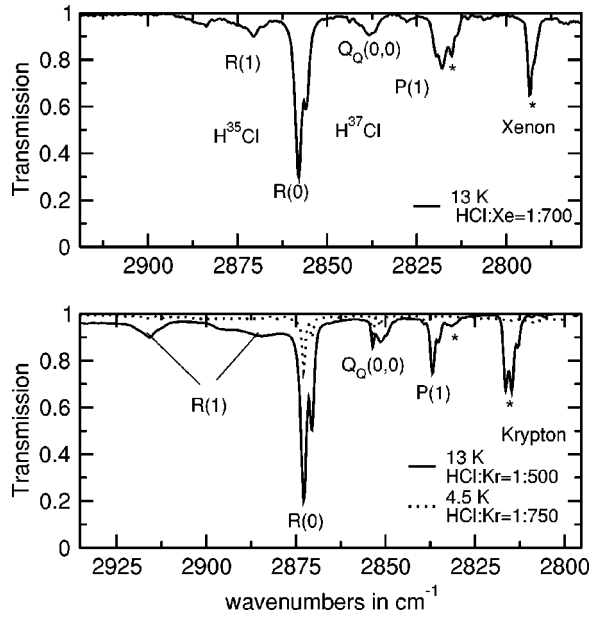

FIG. 1. FTIR absorption spectra $v=0$ to $v=1$ with isotope splitting of $R(0)$ and $P(1)$ bands and additional crystal field splitting of the $R(1)$ branch. The $Q_Q(0,0)$ lines originate from molecules whose rotational motion is distorted and the stars indicate transitions in aggregates. Sample thickness 0.5 mm.

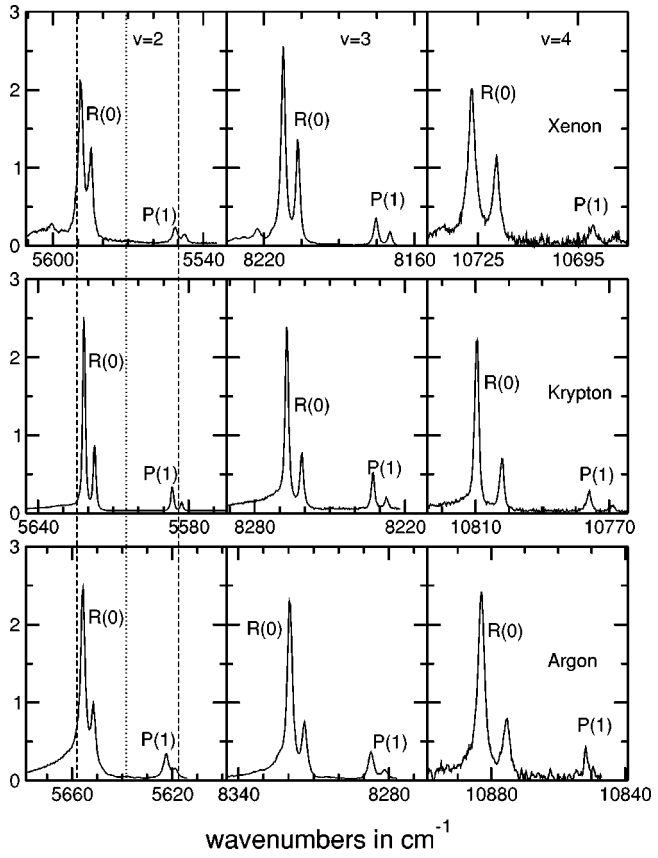

FIG. 2. Overview on the $R(0)$ and $P(1)$ region in the excitation spectra of the overtone excitations $v=0$ to $v=2$, 3, and 4 in Xe, Kr, and Ar detected by the $\Delta v=1$ luminescence. Concentration 1:700, temperature 13 K, sample thickness 0.5 mm.

achieved. Straylight and thermal radiation were blocked by the Ge window of the detector and a bandpass filter for the $\Delta v=1$ fluorescence ($3.4\ \mu m<\lambda<4.2\ \mu m$) which was mounted on the cooling shield of the detector. Thus a detectivity D^* of 8×10^{11} was reached. The time trace from each laser pulse was recorded after amplification by 10^6 in a digital scope and stored on a personal computer for data processing.

III. RESULTS

An overview on the $1\leftarrow0$ absorption in the FTIR spectra is shown in Fig. 1 with the central $R(0)$ and $P(1)$ lines, which are doublets due to the $H^{35}Cl$ and $H^{37}Cl$ isotope splitting. These lines, together with the rotation-free $Q_Q(0,0)$ lines in between will be investigated first with respect to the rotational constants and second to derive the pure vibrational energies. Finally the rotational fine structure at higher energies indicated by $R(1)$ will be treated especially for xenon matrices. The lines at lower energies which are marked by stars originate from dimers and larger aggregates and are well known from concentration studies.[1,12–15] They do not show up in the excitation spectra of the overtone fluorescence obviously due to a low radiative quantum efficiency of these aggregates and are therefore not considered in the following.

Figure 2 presents a collection of the overtone fluorescence excitation spectra for the transitions $v=0$ to 2, 3, and 4 in the three rare gas matrices Xe, Kr, and Ar in the region of the $R(0)$ and $P(1)$ transitions. The comparison of the isotope splittings of the $R(0)$ transition in Fig. 1 with those in Fig. 2 illustrates the higher spectral resolution of 0.1 cm^{-1} in the excitation spectra. A similar comparison with previous data (for example Fig. 2 in Ref. 8) shows better resolved lines in our spectra. The higher resolution and the better absolute accuracy due to the calibration procedure leads to more precise spectral constants in all of the following tables. For the 0 to 2 and 3 transitions we agree within the previous larger error margins with the values of Young and Moore,[8] for the $0\rightarrow4$ transition no previous values are available. The line shapes in Fig. 2 are not instrument limited and the question arises if they are homogeneous or if there is inhomogeneous broadening.[22] We attempted several hole burning experiments in the wings, without observing an effect. Thus we found no indication for inhomogeneous contributions.

A. Rotational constants

The $R(0)$ line corresponds to a transition from $J=0$ in the ground vibrational level to $J=1$ in the excited vibrational level v. The energetic separation between $J=0$ and $J=1$ in v is $2B_v$. $P(1)$ starts from $J=1$ in the ground vibrational level which lies $2B_0$ above $J=0$ and ends in $J=0$ of the vibrational level v. Thus the separation of all pairs of $R(0)$ and $P(1)$ bands in Figs. 1 and 2 is given by $2B_0+2B_v$. Usually only the $v=0$ to 1 transitions of Fig. 1 are available and one would use the rotation free line $Q_Q(0,0)$ to distinguish between B_0 and B_1 because the separation of $Q_Q(0,0)$ and $P(1)$ should yield $2B_0$. The $Q_Q(0,0)$ lines appear only very weakly in the overtone spectra of Fig. 2. Nevertheless one could think to use the $2B_0$ values from Fig. 1 to determine $2B_v$ by subtracting it from the $R(1)$ and $P(1)$ separa-

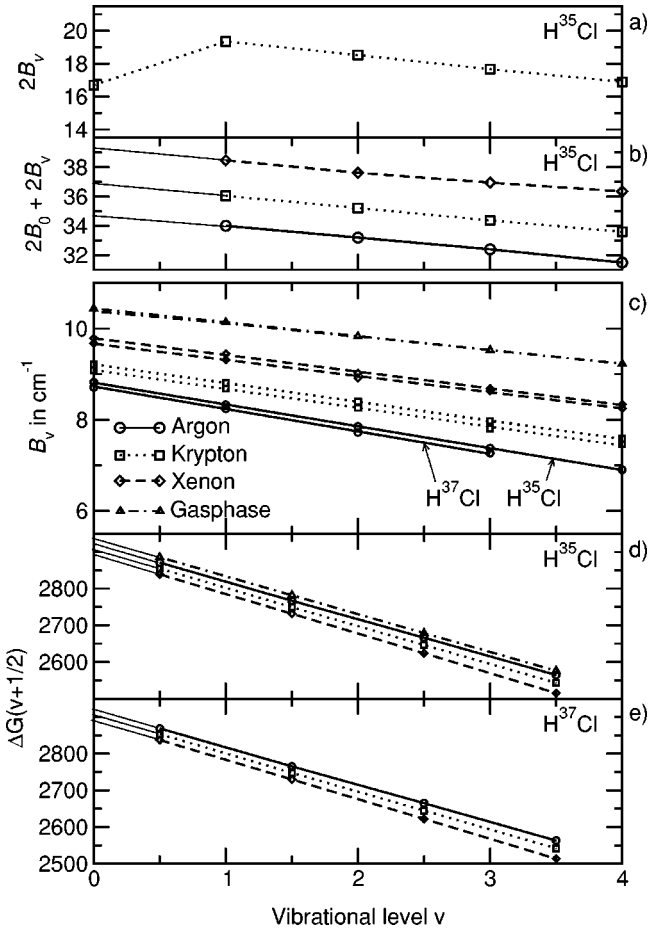

FIG. 3. Illustration of nonsystematic dependence of B_v on v for $H^{35}Cl$ in Kr if the $Q_Q(0,0)$ line from Fig. 1 is used to determine B_0. (b) Extrapolation of the $R(0)-P(1)$ splitting from Fig. 2 which corresponds to $2B_0+2B_v$ and enables the correct derivation of B_0. (c) Linear dependence of B_v on v for all matrices and both isotopes with B_0 from Fig. 3(b) yielding vibration-rotation constants α and B_e [Eq. (1) and Table II]. (d) Birge–Spooner plot of the difference $\Delta G(v)=G(v)-G(v-1)$ of the vibrational energies vs $v+1/2$ according to Eq. (3) for $H^{35}Cl$. (e) Like (d) for $H^{37}Cl$. Same symbols for the matrices are used in (a)–(e).

tions of Figs. 1 and 2. Using this method one obtains the $2B_v$ values which are displayed in Fig. 3(a) for $v=0$ to 4 and $H^{35}Cl$ in Kr, as an example. The initial increase in energy from $2B_0$ to $2B_1$ is in contrast to any expectation. The anharmonicity in the HCl potential leads to an increase in the average HCl bond length, thus to an increase in the moment of inertia and a decrease in $2B_v$ with v. For the nonrigid rotator a linear decrease according to

$$B_v = B_e - \alpha(v+\tfrac{1}{2}) \tag{1}$$

is expected.[23] With the overtone spectra of Fig. 2 we can resolve this discrepancy. In Fig. 3(b) we plot the $R(0)-P(1)$ separation as $2B_0+2B_v$ versus v for $v=1$ to 4 and we extrapolate to $v=0$. The ordinate at $v=0$ yields $4B_0$. Subtracting this $2B_0$ value from the $R(0)-P(1)$ separation yields now indeed the expected linear dependence of B_v on v as it is demonstrated in Fig. 3(c) for the full set of matrices and both isotopes. From the B_v values collected in Table II also B_e and α according to Eq. (1) are derived.

TABLE II. Rotational constants B_v in cm^{-1} for $H^{35}Cl$ and $H^{37}Cl$ in Ar, Kr, and Xe, according to Fig. 3(c) are compared to the gas phase and to Ref. 1. The vibration-rotation coupling constant α and the rotational constant of the equilibrium separation B_e are derived with Eq. (1). The fit uncertainty for α corresponds to 0.01 cm^{-1} and for B_e to 0.03 cm^{-1}.

	Argon		Krypton		Xenon		Gas phase[a]	
	$H^{35}Cl$	$H^{37}Cl$	$H^{35}Cl$	$H^{37}Cl$	$H^{35}Cl$	$H^{37}Cl$	$H^{35}Cl$	$H^{37}Cl$
$(B_0+B_1)/2$[b]	8.7	⋯	8.7	⋯	8.9	⋯	⋯	⋯
B_0	8.83	8.71	9.22	9.09	9.79	9.68	10.44	10.38
B_1	8.33	8.24	8.81	8.69	9.45	9.32	10.14	10.12
B_2	7.85	7.72	8.40	8.27	9.02	8.92	9.83	9.82
B_3	7.36	7.27	7.97	7.81	8.69	8.53	9.53	⋯
B_4	6.90	⋯	7.59	7.46	8.34	8.25	9.23	⋯
α	0.479	0.479	0.41	0.41	0.37	0.34	0.303	0.28
B_e	9.054	8.95	9.42	9.30	9.97	9.85	10.59	10.53

[a]References 23 and 36.
[b]Reference 1.

The failure for the evaluation of B_v by using the $Q_Q(0,0)$ line can be traced to the origin of this line. For a pure vibrational transition of the freely rotating molecule this line is strictly forbidden. It appears in spectra of matrices doped with molecules which experience an anisotropic interaction, for example with other HCl molecules[12–15] or codoped with N_2.[24] Thus the $Q_Q(0,0)$ line belongs to molecules whose rotational motion is additionally hindered by these interactions and therefore it cannot be used to evaluate the $R(0)$ and $P(1)$ branches of molecules in an undistorted surrounding. Therefore we adopted the $Q_Q(0,0)$ notation of Girardet and co-workers[12–15] to indicate that this line originates not from the rotation of undistorted molecules. The comparison in Fig. 3(c) with the gas phase shows a systematic decrease of B_v from the free molecules over Xe to Kr and with the strongest decrease in Ar. Assuming that HCl is placed in a substitutional site then the decrease of B_v correlates inversely with the lattice constant or directly with the tightness of the site. This trend will be attributed in the discussion indeed to a stronger hindering of the rotation in tighter cages. Another feature is the hardly visible rotational isotope effect in the gas phase and its significantly stronger appearance in all matrices for all v values. Table III manifests this effect quantitatively in the different isotope splittings of the $R(0)$ and $P(1)$ lines, which in turn will lead to different $R(0)-P(1)$ separations and thus different B_v values. The rotational isotope effect of the free molecules re-

TABLE III. Isotope splitting of the $R(0)$ and $P(1)$ bands in Figs. 1 and 2 compared with the isotope splitting in the gas phase.

	Argon		Krypton		Xenon		Gas phase[a]
Transition	$R(0)$	$P(1)$	$R(0)$	$P(1)$	$R(0)$	$P(1)$	
1←0	2.00	1.65	2.20	1.70	2.05	1.53	2.01
2←0	4.13	3.60	4.21	3.70	3.78	3.62	4.00
3←0	5.80	5.36	5.91	5.33	5.82	5.61	5.83
4←0[b]	7.50	⋯	7.50	7.0	7.35	7.00	⋯

[a]Reference 23.
[b]Due to the lower S–N ratio of the spectra error in this case 0.3 cm^{-1}.

TABLE IV. Values for the pure vibrational transition energies $G(v)$ from $v=0$ to $v=1$, 2, 3, and 4 with the calculated matrix shift $\Delta\nu$, ω_e and $\omega_e x_e$ according to Eq. (3) in cm^{-1}, error margins are 0.6 and 0.2 cm^{-1}, respectively.

	Argon		Krypton		Xenon		Gas phase
Transition	$H^{35}Cl$	$H^{37}Cl$	$H^{35}Cl$	$H^{37}Cl$	$H^{35}Cl$	$H^{37}Cl$	$H^{35}Cl$
0→1	2871.25	2868.74	2855.28	2853.33	2839.06	2837.25	2885.90
$\Delta\nu$	−14.66	⋯	−30.62	⋯	−46.88	⋯	⋯
0→2	5638.41	5634.04	5604.91	5600.96	5570.78	5566.88	5668.05
$\Delta\nu$	−29.65	⋯	−63.14	⋯	−97.27	⋯	⋯
0→3	8304.75	8298.98	8251.22	8245.64	8194.88	8188.99	8346.98
$\Delta\nu$	−42.23	⋯	−95.76	⋯	−152.1	⋯	⋯
0→4	10869.15	10861.74	10794.43	10787.18	10710.08	10702.30	10923.11
$\Delta\nu$	−53.97	⋯	−128.68	⋯	−213.03	⋯	⋯
ω_e	2970.62	2970.01	2958.49	2956.37	2947.36	2945.36	2988.9
$\omega_e x_e$	51.1	50.9	52.0	51.9	54.0	54.0	52.1

sults from different moments of inertia. The ratio of the B values should scale with ρ^2 according to[23]

$$\frac{B_{H^{35}Cl}}{B_{H^{37}Cl}}=\frac{\mu_{H^{35}Cl}}{\mu_{H^{37}Cl}}=\rho^2, \tag{2}$$

where ρ^2 represents the ratio of the reduced masses μ. In the free molecule ρ amounts to 0.999 24 corresponding to a change in B of 0.15% or about 0.015 cm^{-1}. In the matrices the B values of the heavier isotope lie systematically about 0.15 cm^{-1} lower. The systematic behavior [Fig. 3(a), Table II] gives credibility. This about one order of magnitude larger rotational isotope effect in the matrices yields an additional clue in the discussion on the coupling of the rotation of the matrix cage.

B. Vibrational transitions energies

The spectra in Fig. 2 contain the rovibronic transition energies. With the rotational constants B_0 of Table II it is now possible to extract the pure vibrational energies which are listed in Table IV. The vibrational energies $G(v)$ for a Morse potential follow according to[23]

$$G(v)=\omega_e(v+\tfrac{1}{2})-\omega_e x_e(v+\tfrac{1}{2})^2. \tag{3}$$

The vibrational energies ω_e as well as the anharmonicities $\omega_e x_e$ can be derived from ordinate and slope in a Birge–Spooner plot of $\Delta G(v)=G(v)-G(v-1)$ versus $v+1/2$. The graphs shown in Figs. 3(d) and 3(e) for the two isotopes and the three matrices are linear within experimental accuracy and the resulting ω_e and $\omega_e x_e$ values are included in Table IV. The matrix shifts $\Delta\nu$ are all to the red and the trend is contrary to that of the rotational constants: $\Delta\nu$ increases from Ar to Xe. The trend in $\Delta\nu$ is also reflected in the ω_e values and obviously it does not scale with the size of the cage but with the polarizability of the matrix. $\Delta\nu$ increases also with v. However this behavior is more complex because it originates from the matrix shifts of ω_e and $\omega_e x_e$. $\omega_e x_e$ is larger than the gas phase value in Xe but smaller for Ar. This quantity seems to reflect a competition between the influence of the polarizability and of the cage size.

C. Crystal field splitting of $R(1)$

In the $R(0)$ and $P(1)$ lines only rotational states $J=0$ and 1 are involved. The next higher rotational state $J=2$ shows up in the $R(1)$ line which corresponds to a transition from $J=1$ in the vibrational ground state to $J=2$ in the vibrational state $v=1$, 2, and 3. The $R(1)$ transition is located on the high energy side of $R(0)$ and according to the assignment in Fig. 1 it is split into two bands by the crystal field. The splitting increases from Xe to Kr in accordance with the stronger reduction of the rotational constants in the tighter cage (Table II). Figure 4 presents this rotational fine structure in Xe for the 1←0 FTIR absorption spectrum together with the 2←0 and 3←0 fluorescence excitation spec-

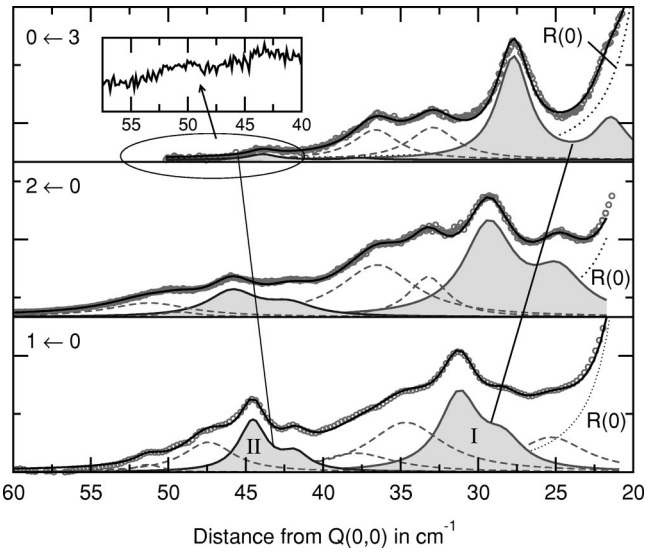

FIG. 4. Rotational structure (circles) in the region of the $R(1)$ branch for the vibrational excitation to the levels $v=1$, 2, 3 in xenon at a temperature of 13 K with a concentration of 1:700 and a sample thickness of 0.5 mm. Energy relative to the pure vibrational transition $Q(0,0)$ calculated by using B_0 from Fig. 3(b). Deconvolution in Lorentzians yields the dotted high energy wing of $R(0)$ and two doublets I and II (shaded). Energy difference between I and II corresponds to $\Delta\nu_c$ in Table V and yields the $T_{2g}-E_g$ splitting in Fig. 5(b) while the energy of band I minus $R(0)$ plus $2B_0$ yields the $T_{2g}-E_g$ transition (ΔI) in Fig. 5(b). The further dashed contributions to the deconvolution are not analyzed.

TABLE V. Energies in cm^{-1} of the doublets I and II of Fig. 4. The energy difference $\Delta\nu_c$ corresponds to the crystal field splitting of $J=2$ and ΔI is given by $I-R(0)+2B_0$ (see text). The isotope splittings $\Delta\nu_{isot}$ are compared with those of $R(0)$.

	I		II				$R(0)$	
	$H^{35}Cl$	$H^{37}Cl$	$H^{35}Cl$	$H^{37}Cl$	$\Delta\nu_c$	ΔI	$H^{35}Cl$	$H^{37}Cl$
0→1	2870.33	2867.48	2883.65	2880.9	13.32	33.90	2857.8	2855.75
$\Delta\nu_{isot}$		2.85		2.75				2.05
0→2	5600.1	5595.6	5616.65	5612.95	16.55	32.60	5588.56	5584.78
$\Delta\nu_{isot}$		4.5		3.7				3.78
0→3	8222.6	8216.3	8244.3	8238.8	21.7	31.53	8212.25	8206.43
$\Delta\nu_{isot}$		6.3		5.5				5.82

tra on an expanded scale. The energy on the *x*-axis is taken relative to the rotation free line $Q(0,0)$. The strong $R(0)$ doublet would be centered at smaller energies and is visible only by its decaying high energy wing. In each of the rather complex experimental spectra (circles) two prominent doublets (shaded) indicated by I and II can be identified. The fitting procedure with Lorentzians yields the same intensity ratio in the doublet I as that of the two isotope components in the $R(0)$ line and also the same splitting. The linewidth FWHM of 2.5–3 cm^{-1} in the doublet I is the same in all spectra and it exceeds that of 2 cm^{-1} in the $R(0)$ line only slightly. In addition a counterpart with the same properties is obtained by fitting. It is marked by II in Fig. 4 (shaded). The doublet II is prominent for the 1→0 transition. It shifts to the blue and decreases in intensity for higher vibrational levels. The bands I and II are attributed to the $R(1)$ transitions of the two isotopes according to the correlations with $R(0)$ and the systematic trend indicated by the lines in Fig. 4. The separation of I and II corresponds to a crystal field splitting $\Delta\nu_c$ of the $J=2$ level. The energy positions of the bands I and II together with $\Delta\nu_c$ are collected in Table V and the rotational isotope splittings $\Delta\nu_{isot}$ are compared with those of the $R(0)$ lines. The remaining contributions to the decomposition of the experimental spectra into Lorentzians are shown as dotted lines for the $R(0)$ wing and as dashed lines for the rest. The dashed contributions are broader and no correlation to $R(0)$ or $R(1)$ bands can be recognized. They belong presumably to phonon side bands of the vibrational transitions[1] and are not considered here further.

IV. DISCUSSION

The survey in Ref. 1 uses the $R(0)-P(1)$ separation as a starting point for the comparison between experiment and theory and concedes reasonable agreement. However we arrive at significantly different experimental values as it is illustrated in the comparison in Table II. The rotational constants B_0 and B_1 in xenon are much larger and closer to the gas phase values compared to the previous data whereas for Ar our mean value of B_0 and B_1 lies below the previous result. Our new results also contain more information due to the availability of the values for B_2, B_3, and B_4 and the systematic behavior gives credibility. Furthermore, the crystal field splitting $\Delta\nu_c$ was considered to be small and of the order of 3 cm^{-1} for DCl. The resulting crystal field barrier of -10 cm^{-1} was treated as a weak perturbation for the interpretation in the model[1] leading to a reduction of the rotational constant by <0.2 cm^{-1}. However, we arrive, even for the weakly interacting xenon matrix where the change in B_0 or B_1 is only 0.6–0.8 cm^{-1} (Table II), at a crystal field splitting of 13–22 cm^{-1} (Table V). Therefore we cannot follow the predominant RTC treatment in Ref. 1 and we analyze the crystal field effects first.

A. Crystal field effects in rotational structure

The free threefold degenerate $J=1$ state remains fully degenerate in fcc or hcp symmetry [no splitting of $R(0)$ and $P(1)$] while the free sixfold degenerate $J=2$ state should split into 2 lines in fcc and into 3 lines in hcp symmetry.[3] The twofold splitting of $R(1)$ (I and II in Fig. 4) demonstrates that the HCl molecule sees the cubic symmetry of the fcc lattice of the matrix and no local hcp contribution has to be invoked. The rotational wave function for $J=0$ of HCl has A_{1g}, and the $J=1$ wave function has T_{1u} symmetry. They remain degenerate in an environment of octahedral symmetry. On the other hand the $J=2$ wave function splits into two states with T_{2g} and E_g symmetry in a fcc environment. Devonshire[3] has calculated the energies E/B of the rotational states in units of the rotational constant B versus the height of the scaled potential K_4/B using the lowest cubic harmonics Y^4 of fourth order to describe the potential. Therefore the electrostatic energy V_4 is given in this case by

$$V_4 = K_4\left(P_4^0(\cos\theta) + \frac{1}{168}P_4^4(\cos\theta)\cos 4\phi\right) \tag{4}$$

and is shown in Fig. 5(a). The value of $2B_v$ in Xe from Table II taken in units of B_v from the gas phase corresponds to the $A_{1g}-T_{1u}$ or $(J=0\rightarrow 1)$ transition of Fig. 5(a). The energy ΔI of the next higher transition $R(1)$ going from $J=1$ (T_{1u}-symmetry) to $J=2$ (E_g symmetry) can be calculated by subtracting from the energy of band I the energy of $R(0)$ (Table V) and adding the energy of $2B_0$ from Table II. The values $\Delta I = I - R(0) + 2B_0$ are presented in Table V. The obtained values have to be scaled with B_v from the gas phase (Table II), too. Finally, the $T_{2g}-E_g$ splitting of $J=2$ corresponds to $\Delta\nu_c$ in Table V after scaling by B_v. We entered the diagram of Fig. 5(a) with these scaled energies. However, it is not possible to find a value of the barrier height K_4/B which is consistent within reasonable limits with the three conditions.

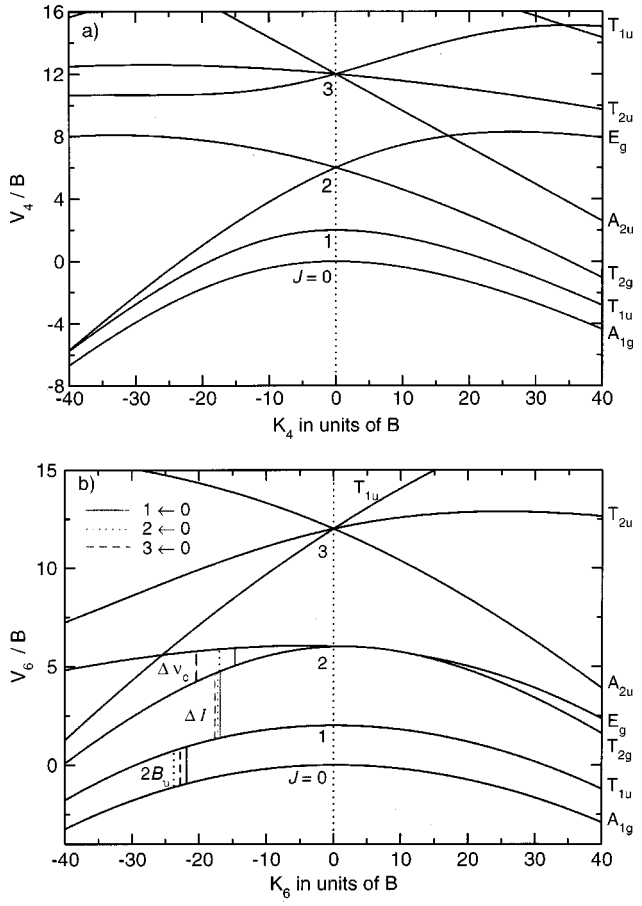

FIG. 5. (a) Electrostatic energy V_4 vs the barrier height K_4 in units of the rotational constant B according to Eq. (4). (b) V_6 vs K_6 dependence from Eq. (5). The optimal K_6/B values for the experimental $\Delta\nu_c$ and ΔI energies (from Fig. 4) are shown for the three vibrational transitions $0\rightarrow1$, 2, 3 together with $2B_v$ from Table III. All values are normalized to the rotational constant of the gas phase. For the assignment, see text.

This observation is consistent with calculations for the potential field of the HCl molecule in matrices which indicate strong contributions of the next higher harmonics Y^6.[10,11] The electrostatic energy V_6 for this term follows according to[25]

$$V_6 = K_6 \tfrac{1}{4}(\sqrt{2}P^0_{6\cos} - \sqrt{14}P^4_{\cos}), \tag{5}$$

with

$$P^0_{6\cos} = \sqrt{\frac{18}{8\pi\cdot 6!}}\, 2\cos(\phi)\times Y^0_6,$$

$$P^4_{6\cos} = \sqrt{\frac{14}{8\pi\cdot 10!}}\, 2\cos(\phi)\times Y^4_6.$$

The energy V_6/B versus K_6/B is displayed in Fig. 5(b). The experimental results are much more consistent with the V_6 diagram. The three observed scaled energies (indicated by $2B_v$, ΔI, and $\Delta\nu_c$) are shown at the optimal K_6/B values for the fundamental ($v=0\rightarrow1$) and the two overtones ($v=0\rightarrow2$ and 3). The K_6/B values are distributed over a range of 15–23. Some systematic trends can be read from Fig. 5(b). All three $A_{1g}-T_{1u}$ transitions lie closely together around $K_6/B\approx22$. In Sec. IV B we will show that the eccentric motion reduces $2B_v$ in addition to the crystal field effects discussed here. The crystal field effect alone would correspond to a somewhat larger $2B_v$ which would shift the correct K_6/B in the direction of ΔI and $\Delta\nu_c$. The T_{1u} and the A_{1g} branches are rather parallel and approach each other very slowly with increasing K_6/B. Therefore this transition is not very sensitive to K_6 and a minor additional contribution may lead to a large shift.

The $T_{1u}-E_g$ (ΔI) and the $T_{2g}-E_g$ ($\Delta\nu_c$) separations on the other hand change much more rapidly with K_6/B and are better suited to determine the barrier height. The three values of ΔI are well centered on $K_6/B=17$ with a very weak trend of an increase from $v=1$ to $v=3$. The mean value for $\Delta\nu_c$ corresponds to the same K_6/B. However, the trend from $v=1$ ($K_6/B=13$) to $v=3$ ($K_6/B=20$) is more pronounced. The anharmonicity of the intramolecular HCl potential (Table IV) leads to an expansion of the molecule, also evident from α [Eq. (3), Table II]. Therefore the rotating molecule interacts more strongly with the cage and a systematic increase of K_6/B with v can be expected. However, the different ranges of K_6/B values arising from ΔI and $\Delta\nu_c$ can originate also from some contributions of V_4. Beyeler[2] has treated the solutions for a superposition of V_4 and V_6, but, for a too coarse variation of the relative weights and for a different normalization. Therefore we repeated the calculations for a continuous variation of the strength of K_4 and K_6 in the same normalization. Now we show in Fig. 6 the potential sheets for

$$V = K_4V_4 + K_6V_6 \tag{6}$$

once more in units of B for the three branches of $J=0$ (A_{1g}), $J=1$ (T_{1u}) states and $J=2$ which is split in the substrates T_{2g} and E_g. In analogy to Fig. 5 we search for the combinations of K_4 and K_6 values for which the energy differences between the sheets correspond to the experimental transition energies. The $A_{1g}-T_{1u}$ transitions are not considered due to the same reason as in the pure V_6 case. The $T_{2g}-E_g$ transitions lead to one set of three lines ($v=1$, 2, and 3) in Fig. 7 and these for the $T_{2g}-E_g$ transition to another one. The crossings for the same v yield the searched solutions. Inspection of the solutions which are marked by dotted horizontal lines shows that the K_6/B values fall again in a range of 13 to 23, whereas the K_4/B values are much smaller covering a range of 0–3. Thus it is confirmed that the V_6 term dominates by far the interacting potential and that the barrier height has to be of the order of 17 B_v. The V_4 contribution may give an interesting indication that the symmetry of the potential field is rather sensitive to the size of the molecule. We see that the trend of K_6 with v is reversed and K_6 decreases from 23 to 13 in going from the smaller extension in $v=1$ to the larger one in $v=3$.

The reduction in K_6 however is compensated by K_4 which increases from 0 to 3 in going from $v=1$ to $v=3$. The reason can be the structure of the first and second shell of cage atoms. The structure scheme in Fig. 8(a) shows the definition of the angles ϕ and θ for the orientation of the molecules in the substitutional site. In addition, the numbered positions 1 to 12 of the cage atoms in the first shell are indicated. The angular plot of the V_6 potential in Fig. 8(b)

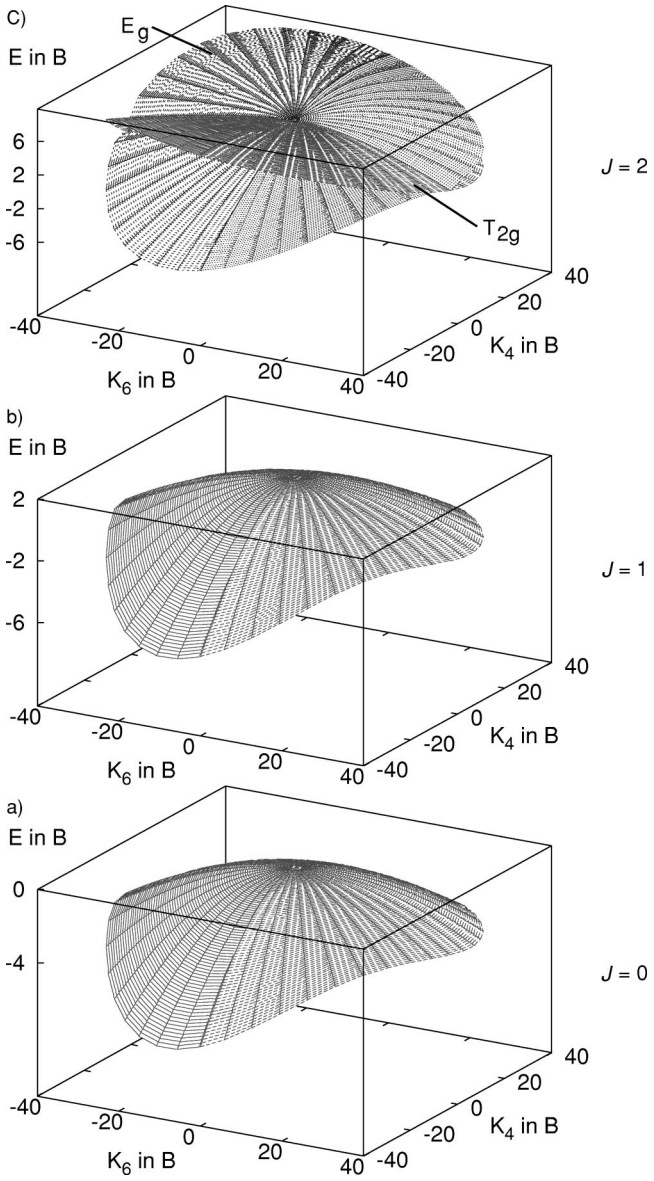

FIG. 6. Two-dimensional plot of the electrostatic energy V/B vs K_4/B and K_6/B according to Eq. (6) with (a) $J=0$ (A_{1g}-symmetry); (b) $J=1$ (T_{1u}-symmetry); and (c) $J=2$ (T_{2g} and E_g-symmetry).

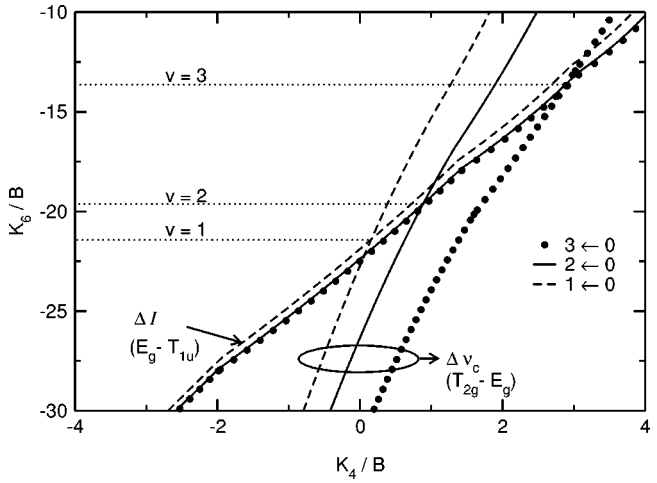

FIG. 7. The strong symbols follow the energy differences between the lower sheet in Fig. 6(b) and the two upper sheets in Fig. 6(c) which are chosen according to the normalized $\Delta\nu_c$ and ΔI in analogy to the one-dimensional plot Fig. 5. The crossings deliver the pairs of K_6/B and K_4/B values consistent with experimental $T_{2g}-T_{1u}$ and $T_{2g}-E_g$ transition energies. Three sets of lines due to the $v=0\rightarrow1$ (dashed) $v=0\rightarrow2$ (solid) and the $v=0\rightarrow3$ (dotted) vibrational transition are obtained and the three K_6 values are marked by weak dotted horizontal lines.

illustrates the repulsive maxima if the molecule points to these 12 cage atoms. The different sign for K_4 and K_6 (Fig. 7), yields for the V_4 potential in Fig. 8(c) repulsive maxima just for the positions of the second shell of cage atoms. If we accept the trend that the combined potential V depends on v then we can conclude that HCl in the higher vibrational states interacts already slightly with the noble gas atoms of the second shell. Their repulsive behavior is expressed by the potential V_4 with $Y^4_{A_{1g}}$ symmetry. However, further experimental confirmation may be necessary because we have the problem of additional contributions to B_v discussed in Sec. IV B.

Apart from these detailed symmetry considerations we obtain for an average $K_6/B\approx17$ a barrier height of 160 cm^{-1}. It is more than one order of magnitude larger than the values considered in Ref. 1 which is expected according to the very different new experimental data. The values from Ref. 24 with 170 cm^{-1} for Kr and 280 cm^{-1} for Ne come closer to our data. Theoretical values span a broad range from 800 cm^{-1} for Ar (Refs. 6 and 9) to 60 cm^{-1} for Ar.[9,25] The rather low values in Refs. 25 and 26 may be related to the HCl–Ar potential used.[27,28] These calculations reproduce the vibrational energy of the fundamental transition much better than that of the first overtone. It may be an indication that the potential is less accurate at larger elongations which are relevant for the rotational barriers.

B. Contributions form eccentric motion

Until now we focused our attention on the most prominent effect which originates from the hindering of the rotation by the barriers in the crystal field and which accounts for the larger part of the reduction of the rotational constant at least in Xe. However, further contributions originating, especially from the separation a between the center-of-mass and the center of interaction may well be present especially in Kr and Ar, where the crystal field effects were not analyzed. The resulting eccentric rotation leads itself to an increase in the moment of inertia named I_1 and it causes a pseudorotation of the cage[18] with I_2 and a RTC contribution[1] with I_3. A molecule with a total mass M which rotates around an axis separated by a from the center-of-mass experiences an additional moment of inertia of

$$I_1 = M\times a^2. \tag{7}$$

Estimates of a differ considerably. For Ar values between 0.1–0.4 Å (Refs. 1, 9, and 12) are discussed and the most accepted one lies around 0.1 Å. For Xe a smaller value seems plausible due to the larger substitutional cage size. If we take $a=0.05$ Å for a first estimate then we arrive at $I_1 = 0.15\times10^{-47}$ kg m^2 which corresponds to an increase by 5% relative to the gas phase value of $I=2.697\times10^{-47}$ kg m^2 and a similar decrease in the rotational con-

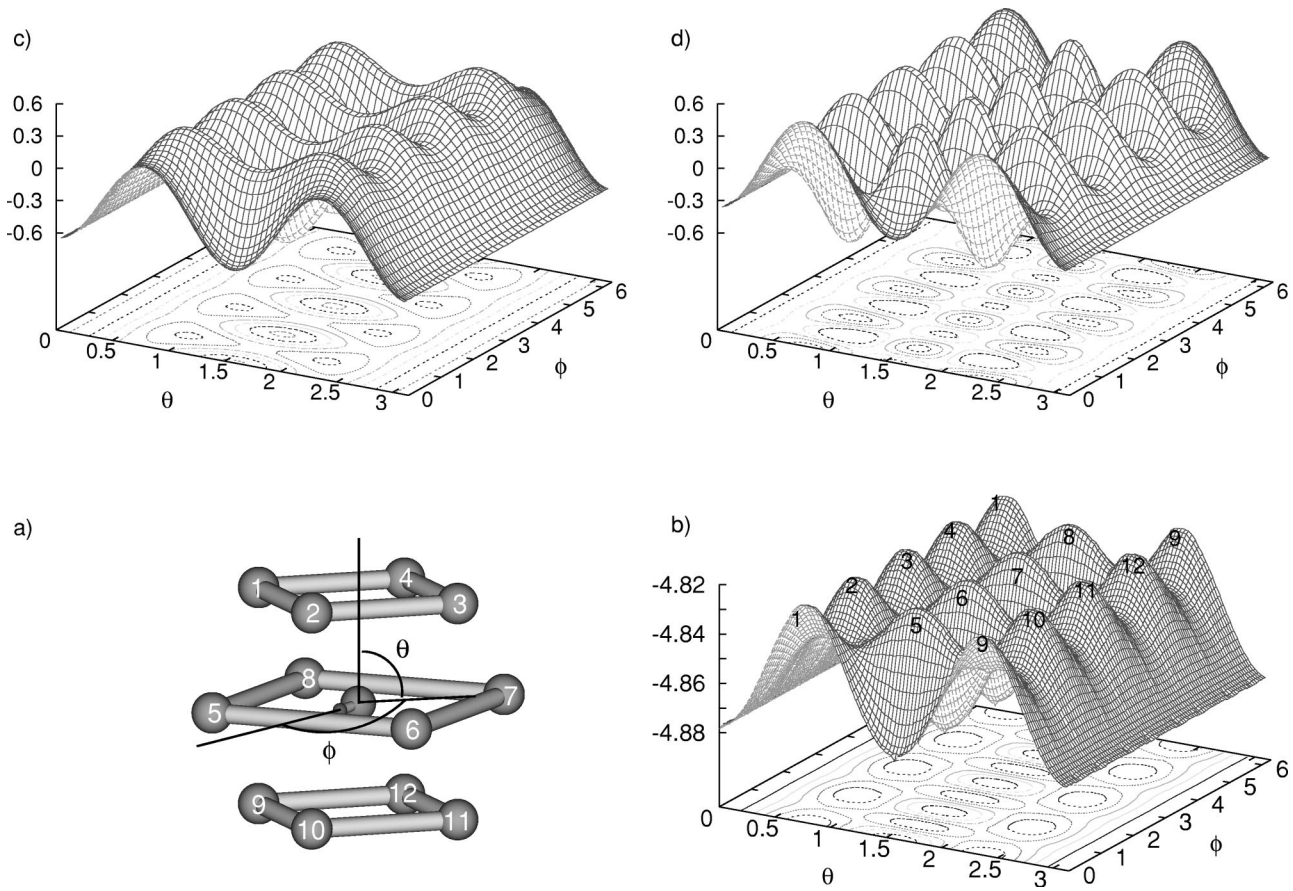

FIG. 8. (a) Scheme of angular coordinates θ, ϕ and numbered positions of the first shell of matrix atoms around the substitutional embedded HCl in the noble gas fcc lattice. (b) Plot of V_6 vs θ and ϕ according to Eq. (5) with the maxima at the positions of the cage atoms. (c) Like (b) for V_4 and Eq. (4). (d) HCl-potential determined by a DIM-calculation using the H–Xe pair potential of Toennies and Tang (Ref. 31) and Xe–Cl potentials of Aquilanti *et al.* (Ref. 29).

stant B_v. The average difference of B_v in Xe to the gas phase for $H^{35}Cl$ amounts to a reduction by $\approx 0.8\ cm^{-1}$ or 8% according to Table II. The reduction of B_v by the crystal field in the $T_{1u}-A_{1g}$ transition in Fig. 5(b) for $K_6/B=17$ [consistent with the $R(1)$ branch splitting] yields a reduction by 4%. Thus the I_1 contribution together with the crystal field effect results in a reduction by 9% in reasonable agreement with the observation of 8% in view of the crude estimate. The eccentric motion causes also an isotope effect and the change ΔI_1 in Eq. (7) for $H^{35}Cl$ to $H^{37}Cl$ is obtained by $\Delta M=2$. The derived isotope effect results in $0.03\ cm^{-1}$ which goes in the right direction. However, it is smaller than the observed isotope effect in Xe of $0.11\ cm^{-1}$ (Table II). For the pure crystal field model it is not expected that the isotope effect should differ from the gas phase at all. Therefore the isotope effect and the I_1 contribution to B_v strongly suggest an additional contribution by the eccentric motion. To achieve a more quantitative agreement, and to disentangle also I_2 and I_3 contributions, it will be necessary to treat the crystal field and RTC contributions in a more advanced self-consistent way.

C. Vibrational energies

It has already been mentioned that the fundamental vibrational energy in Ar was reproduced by a diatomic-in-molecule calculation (DIM) with remarkable accuracy.[25,26] We tried to extend the calculations to higher overtones and to other matrices in adopting the program within a collaboration. However, a problem with the available pair potentials has been recognized. For Ar it was possible to use the angle dependent HCl–Ar potentials of Hutson.[27,28] These are not available for Kr and Xe. To be consistent, we used for all three matrices a combination of Cl-rare gas potentials of Aquilanti[29,30] and H-rare gas potentials of Toennies and Tang[31] in analogy to previous calculations.[32–34] A comparison of our result with those using the Aquilanti potentials[30] showed a severe discrepancy in the three-dimensional potential energy surface. The symmetry was the same, but for example the barrier for rotation amounted in our case to 800 cm^{-1}, whereas the published value with the angular dependent potential is 60 cm^{-1}.[25] Allowing for a pseudorotation of the matrix atoms by optimizing the geometry with the steepest descent method reduced the barrier to 450 cm^{-1}. A plot of the calculated angular distribution of the potential is shown in Fig. 8(d). The potential is in agreement with the predominant $Y^6_{A_{1g}}$ symmetry according to the similarity with Fig. 8(b). Nevertheless, we consider the discrepancy as too large to attempt a reliable calculation of vibrational energies in Xe and Kr matrices. It should be kept in mind that the calculation with the Hutson potential in Ar was also less convincing

for the overtones. There is a more general notion that the admixture of ionic contributions for example in a DIIS scheme[35] has to be included in a more systematic way.

ACKNOWLEDGMENTS

The experimental help by Mrs. Ramona Weber and the fruitful discussions with Professor Apkarian are gratefully acknowledged. This work was funded by the Deutsche Forschungsgemeinschaft in the Sonderforschungsbereich 450.

[1] H. Hallam, *Vibrational Spectroscopy of Trapped Species* (Wiley, New York, 1973).
[2] U. Beyeler, J. Chem. Phys. **60**, 4123 (1974).
[3] A. F. Devonshire, Proc. R. Soc. London, Ser. A **153**, 601 (1936).
[4] P. Mannheim and H. Friedmann, Phys. Status Solidi **39**, 409 (1970).
[5] H. Shin, J. Chem. Phys. **75**, 3821 (1981).
[6] A. Cenian and H. Gabriel, Chem. Phys. **123**, 113 (1988).
[7] J. Wiesenfeld and C. Moore, J. Chem. Phys. **70**, 930 (1979).
[8] L. Young and C. Moore, J. Chem. Phys. **81**, 3137 (1984).
[9] S. Henning, A. Cenian, and H. Gabriel, Chem. Phys. Lett. **205**, 354 (1993).
[10] F. Neugebauer and V. May, J. Chem. Phys. **107**, 205 (1999).
[11] J. Manz, P. Saalfrank, and B. Schmidt, J. Chem. Soc., Faraday Trans. **93**, 957 (1997).
[12] C. Girardet and D. Maillard, J. Phys. Chem. **77**, 5923 (1982).
[13] D. Maillard, H. Shriver, J. P. Perchard, and C. Girardet, J. Phys. Chem. **71**, 505 (1979).
[14] D. Maillard, H. Shriver, J. P. Perchard, and C. Girardet, J. Phys. Chem. **71**, 517 (1979).
[15] C. Girardet and D. Maillard, J. Phys. Chem. **77**, 5941 (1982).
[16] B. Laroui, J. P. Perchard, and C. Girardet, J. Phys. Chem. **97**, 2347 (1992).
[17] L. Keyser and G. Robinson, J. Chem. Phys. **45**, 1694 (1966).
[18] J. Manz, J. Am. Chem. Soc. **102**, 1801 (1979).
[19] N. Rao, *Molecular Spectroscopy: Modern Research* (Academic, New York, 1976), Vol. IIa.
[20] W. Holle and D. Robinson, J. Chem. Phys. **53**, 3768 (1970).
[21] U. Brackmann, *Lambdachrome Laser Dyes* (Lambda Physik, Göttingen, 1986).
[22] C. Crepin, M. Broquier, H. Dubost, J. Galaup, J. LeGouet, and J. Ortega, Phys. Rev. Lett. **85**, 964 (2000).
[23] G. Herzberg, *Molecular Spectra and Molecular Structure I. Spectra of Diatomic Molecules* (Van Nostrand, New York, 1950).
[24] M. T. Browers and W. H. Flygare, J. Chem. Phys. **44**, 1389 (1966).
[25] B. Schmidt, *Making and Breaking of Chemical Bonds: Dynamics of Elementary Reactions From Gas Phase to Condensed Phase* (Habilitation, FU-Berlin, 1998).
[26] B. Schmidt and P. Jungwirth, Chem. Phys. Lett. **259**, 62 (1996).
[27] J. Hutson and B. Howard, Mol. Phys. **43**, 493 (1981).
[28] J. M. Hutson, J. Chem. Phys. **81**, 2357 (1984).
[29] V. Aquilanti, D. Cappelletti, V. Lorent, E. Luzzatti, and F. Pirani, Chem. Phys. Lett. **192**, 153 (1992).
[30] V. Aquilanti, D. Cappelletti, V. Lorent, E. Luzzatti, and F. Pirani, J. Phys. Chem. **97**, 2063 (1993).
[31] K. Tang and J. Toennies, Chem. Phys. **156**, 413 (1991).
[32] I. Gersonde and H. Gabriel, J. Chem. Phys. **98**, 2094 (1993).
[33] A. Krylov and R. Gerber, Faraday Discuss. **108**, 243 (1997).
[34] A. Krylov, R. Gerber, and R. Coalson, J. Chem. Phys. **105**, 4626 (1996).
[35] I. Last and T. F. George, J. Chem. Phys. **89**, 3071 (1988).
[36] G. Herzberg and J. Spinks, Z. Phys. **89**, 474 (1934).